

# Anharmonic Cation–Anion Coupling Dynamics Assisted Lithium-Ion Diffusion in Sulfide Solid Electrolytes

Zhenming Xu, Xi Chen, Hong Zhu, and Xin Li\*

Sulfide-based lithium superionic conductors often show higher Li-ion conductivity than other types of electrolyte materials. This work unveils a unique Li-ion conductive behavior in these materials through the perspective of anharmonic coupling assisted Li-ion diffusion. Li hopping events can happen simultaneously with various types of lattice dynamics, while only a statistically important synchronization of motions may indicate coupling. This method enables a direct evaluation of the coupling strength between these motions, which more fundamentally decides if a specific type of lattice motion is really anharmonically coupled to the Li hopping event and whether the coupling can facilitate the Li diffusion. By a new *ab initio* computational approach, this work unveils a unique phenomenon in prototype sulfide electrolytes in comparison with typical halide ones, that Li-ion conduction can be boosted by the anharmonic coupling of low-frequency Li phonon modes with high-frequency anion stretching or flexing phonon modes, rather than the low-frequency rotational modes. The coupling pushes Li ions toward the diffusion channels for reduced diffusion barriers. The result from the lower temperature range ( $\approx 0$ –300 K) of simulation can also be more relevant to the application of solid-state batteries.

## 1. Introduction

Sulfide-based lithium ionic conductors often show higher ionic conductivities than the oxides and organic polymers and have excellent mechanical properties for compatibility with scaling-up engineering procedures, negligible grain-boundary resistance, and synthesis convenience at low temperature.<sup>[1–3]</sup> Therefore, the sulfide-based lithium ionic conductors are promising solid-state electrolyte materials to replace the commercial liquid electrolytes and polymer separators, which may also effectively combine with lithium metal anode without dendrite

penetration,<sup>[4,5]</sup> increasing the safety and energy density of solid-state batteries.

As to one of the most important performance metrics of ionic conductivity, a deeper understanding of the physical origin of fast ion transport in existing electrolytes is the key to further design advanced superionic conductors. Previous pioneering works have mainly focused on three aspects to help understand Li (or Na) diffusion mechanisms in these materials: crystal structure or static mechanical property,<sup>[6–8]</sup> concerted cation diffusion,<sup>[9,10]</sup> and ion-lattice interaction dynamics.<sup>[11–22]</sup> For the ion–lattice interaction, three main categories of interaction mechanisms were discussed on the paddle wheel effect,<sup>[13–15,22]</sup> the soft phonon related effects,<sup>[11,17,21]</sup> and anharmonic effect,<sup>[16,23,24]</sup> respectively.


In 1972, a model was proposed to connect the high ionic conductivity of Li ions with polyanion rotational disordering in  $\alpha$ -Li<sub>2</sub>SO<sub>4</sub><sup>[25]</sup> in the temperature range of  $\approx 635$ –790 °C. The model proposes that

tetrahedral SO<sub>4</sub><sup>2-</sup> polyanion rotation can widen the diffusion pathway for Li-ion hopping, eventually increasing lithium ionic conductivity, which is also called the “paddle-wheel” mechanism.<sup>[26,27]</sup> The rotational behavior of SO<sub>4</sub><sup>2-</sup> polyanion was later observed by neutron diffraction experiments at 650 °C.<sup>[28]</sup> Although similar effect was also reported in other sulfate and borohydride phases with fast alkali metal ion conduction in high or medium temperature ranges, such as LiNaSO<sub>4</sub>,<sup>[29]</sup> LiAgSO<sub>4</sub>,<sup>[29]</sup> LiBH<sub>4</sub>,<sup>[30]</sup> Li<sub>2</sub>B<sub>12</sub>H<sub>12</sub>,<sup>[31]</sup> and Na<sub>2</sub>B<sub>12</sub>H<sub>12</sub>,<sup>[31,32]</sup> there was actually an intensive debate about the effect especially in the sulfates,<sup>[33–36]</sup> partly because the direct observation of such an ultrafast dynamic effect on the atomic scale is challenging in both experiment and computation. For example, *ab initio* molecular dynamics (AIMD) simulation could not find sufficient Li hopping events well correlated with SO<sub>4</sub> rotation events simultaneously, although the rotation of polyanion was observed in the simulation.<sup>[36]</sup> Meanwhile, the work discussed the complexity of lattice dynamics beyond polyanion rotation in Li<sub>2</sub>SO<sub>4</sub> and suggested the importance of inelastic neutron diffraction for a further study.

Furthermore, recent investigations of the paddle-wheel phenomenon in sulfide electrolytes were mostly in high-temperature crystalline phases with large free volume for polyanion rotation, such as Li<sub>3.25</sub>P<sub>0.75</sub>Si<sub>0.25</sub>S<sub>4</sub><sup>[14]</sup> and Na<sub>3</sub>PS<sub>4</sub>,<sup>[22]</sup> although there was one report of the effect in glass 0.75Li<sub>2</sub>S–0.25P<sub>2</sub>S<sub>5</sub><sup>[13]</sup> at room temperature. In addition, although experiments like X-ray

Z. Xu,<sup>[†]</sup> X. Chen, X. Li  
John A. Paulson School of Engineering and Applied Sciences  
Harvard University  
Cambridge, MA 02138, USA  
E-mail: lixin@seas.harvard.edu

Z. Xu, H. Zhu  
University of Michigan–Shanghai Jiao Tong University Joint Institute  
Shanghai Jiao Tong University  
800 Dongchuan Road, Shanghai 200240, P. R. China

 The ORCID identification number(s) for the author(s) of this article can be found under <https://doi.org/10.1002/adma.202207411>.

<sup>[†]</sup>Present address: College of Materials Science and Technology, Nanjing University of Aeronautics and Astronautics, Nanjing 210016, P. R. China

DOI: 10.1002/adma.202207411

and neutron diffractions can detect the existence of polyanion rotation, the direct correlation of the rotation with Li-ion hopping event is more challenging and often has to resort to AIMD. We notice that the reported AIMD result of  $\text{Li}_{3.25}\text{P}_{0.75}\text{Si}_{0.25}\text{S}_4$ <sup>[14]</sup> was at >600 K and that of  $\text{Na}_{11}\text{Sn}_2\text{PX}_{12}$  ( $X = \text{S}$  and  $\text{Se}$ )<sup>[15]</sup> was at >500K, when the paddle-wheel effect was discussed. For these crystalline phases of superionic conductors, the large free volume and/or kinetic energy of atoms in the high temperature phases may make the rotation prominent. However, it has been discussed widely in the field that extrapolating high temperature computations to project room temperature behavior may cause problems.<sup>[37]</sup> Although polyanion rotation may persist down to low temperature ( $\approx 0$ –300 K) for certain types of materials,<sup>[14,15]</sup> whether the rotation can help Li-ion diffusion is less investigated in this low temperature range of more relevance to the application in solid state batteries. In other words, exploiting the effect near room temperature still presents a great challenge.

On the other hand, some recent works emphasized the effect of the soft phonon on activation energy barrier and cation conduction, mainly based on low temperature ( $\approx 0$ –300 K) measurement and computation. The softer lattice dynamics or higher lattice polarizability gives lower frequency for the center of lithium phonon density of states (DOS), which was found to show a nice correlation with smaller activation energy barrier and higher Li-ion conductivity in  $\text{Li}_3\text{PO}_4$ -based LISICON,  $\text{Li}_6\text{PS}_5\text{X}$  ( $X = \text{Cl}, \text{Br}, \text{I}$ )-based argyrodite, and  $\text{Na}_3\text{PS}_{4-x}\text{Se}_x$  families.<sup>[11,17–19,21]</sup> It is worth noting that such a material-dependent descriptor, as far as we know, has not been found yet based on the paddle-wheel effect. The soft phonon effect<sup>[12,19,21]</sup> was further discussed within the scope of Meyer–Neldel rule,<sup>[38]</sup> emphasizing the importance and complexity of entropy and lattice vibrational spectrum on the ion diffusion. Particularly, soft phonon increases the cation oscillation amplitude for a higher hopping probability,<sup>[11,18,39]</sup> while simultaneously soft lattice also decreases the oscillator frequency and the attempt frequency of the hopping event.<sup>[17,21]</sup> Related to this complicated tradeoff effect, a study also suggests that the descriptor should be used for structurally and chemically similar conductors after studying broader families of electrolytes.<sup>[12]</sup> For example, although sulfides often show superior ionic conductivity than halides, it was found that sulfides usually also show higher frequency of lithium phonon band centers than halides.<sup>[20]</sup>

Although crystal anharmonicity is often considered to be equivalent to lattice softness, they emphasize different aspects. Especially, the anharmonic phonon coupling effect can couple different modes in a wide frequency range for advanced phenomena, as recently discussed in strongly correlated crystalline materials of cuprate superconductors.<sup>[40–42]</sup> As to superionic conductors, Delaire et al. recently emphasized the importance of anharmonic phonon effect on ionic and heat conduction in Cu-ion,<sup>[24]</sup> Ag-ion,<sup>[23]</sup> and Na-ion<sup>[16]</sup> electrolytes, where low-frequency broad peaks at a few meV were observed from inelastic neutron scattering measurements at room and lower temperatures, attributed to complicated motions of cations (i.e., Cu, Ag, or Na ions). For  $\text{Na}_3\text{PS}_4$ <sup>[16]</sup> the possibility of coupling Na-ion diffusion with other motions of  $\text{PS}_4$  units beyond rotation was suggested from their AIMD simulations, because freezing rotation of  $\text{PS}_4$  was found to show little influence on the calculated

Na phonon DOS while freezing all motions of  $\text{PS}_4$  did show significant change of the DOS. In addition, among these non-rotational motions, a type of low frequency wiggling motion of  $\text{PS}_4$  was particularly mentioned.

In this work, borrowing from an ab initio computational method that was recently developed to calculate the anharmonic coupling effect in strongly correlated materials,<sup>[40,41]</sup> we were able to directly investigate all the anharmonic phonon couplings at 0 K for superionic conductors, which allows us to articulate the types of mode couplings in these electrolyte materials for the first time. Further combined with AIMD evaluation of ionic conductivity and vibrational phonon DOS (VDOS) at 300 K, we obtain an understanding that is more relevant to the temperature range of interest to the practical application of these materials in solid state batteries. We unveil a relationship between anharmonic phonons and Li-ion conduction in a few representative sulfide and halide solid electrolytes, including  $\text{Li}_7\text{P}_3\text{S}_{11}$ ,  $\text{Li}_{10}\text{GeP}_2\text{S}_{12}$ ,  $\beta\text{-Li}_3\text{PS}_4$ ,  $\text{Li}_3\text{YBr}_6$  (space group: C2/c), and  $\text{Li}_3\text{ErCl}_6$  (space group: P321). Specifically, we find that for sulfide-based lithium superionic conductors, the smaller activation energy barrier of Li diffusion is often related to the asymmetric redistribution of Li VDOS more toward the low-frequency vibrational direction, driven by the anharmonic coupling with high-frequency anion stretching or flexing modes, rather than the low-frequency rotational modes. Through such an anharmonic phonon coupling, Li ions are pushed by the modes moving toward the diffusion channel for a reduced diffusion barrier. In contrast, such a redistribution is largely symmetric toward high- and low-frequency directions in halide electrolytes that we evaluated. Further understanding along this direction may provide a new route to design superionic conductors with higher alkaline ion conductivity for solid state battery applications.

## 2. Results and Discussion

VDOS from the room temperature AIMD simulations includes the anharmonicity and temperature effects,<sup>[12]</sup> reflecting the cation–anion coupling dynamics that is usually not included by conventional phonon calculations if the anharmonic effect is not explicitly considered. We performed the AIMD simulations at 300 K for some typical lithium ionic conductors, including  $\text{Li}_7\text{P}_3\text{S}_{11}$ ,  $\text{Li}_{10}\text{GeP}_2\text{S}_{12}$ ,  $\beta\text{-Li}_3\text{PS}_4$ ,  $\text{Li}_3\text{YBr}_6$ , and  $\text{Li}_3\text{ErCl}_6$ , and calculated the corresponding Li projected VDOS. To explore and separate the contribution from cation–anion coupling dynamics to VDOS, AIMD simulations were performed under two different conditions of fixing polyanions and no constraints, respectively, corresponding to cases without and with cation–anion coupling, as shown in **Figure 1**.

The Li VDOS redistributes upon cation–anion coupling, where the number of medium-frequency Li vibration modes decreases, and the number of both low-frequency ( $N_{\text{low}}$ ) and high-frequency ( $N_{\text{high}}$ ) modes increases. To quantitatively compare such redistribution of VDOS toward high and low frequency directions upon the coupling, we take their difference ( $N_{\text{low}} - N_{\text{high}}$ ) for these materials and find a reversed correlation with their activation energy barriers ( $E_a$ ), as presented in **Figure 1f**. A larger value of  $N_{\text{low}} - N_{\text{high}}$  means that the increase

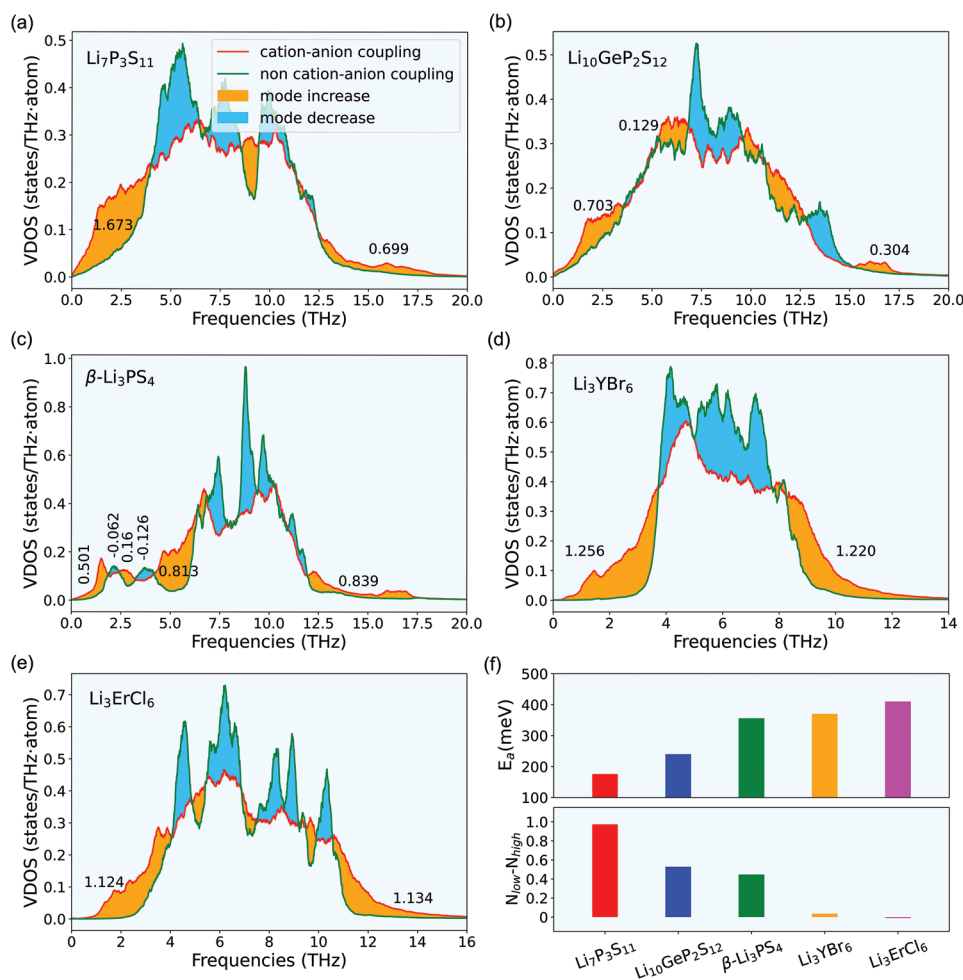


**Figure 1.** a–e) Vibrational density of states (VDOS) of Li ions from AIMD simulations at 300K for  $\text{Li}_7\text{P}_3\text{S}_{11}$ ,  $\text{Li}_{10}\text{GeP}_2\text{S}_{12}$ ,  $\beta\text{-Li}_3\text{PS}_4$ ,  $\text{Li}_3\text{YBr}_6$ , and  $\text{Li}_3\text{ErCl}_6$ , respectively. The red and green curves are Li VDOS with and without cation–anion coupling. The orange and blue areas represent the VDOS redistributions upon cation–anion coupling. The effect of such redistribution is quantified by a weighted VDOS integral  $N = \int \text{VDOS} \cdot (f_{\text{center}} - f) df$ , where  $f_{\text{center}}$  is the weighted center of the total VDOS without cation–anion coupling; f) the weighted mode number difference ( $N_{\text{low}} - N_{\text{high}}$ ) between the low- and high-frequency ranges upon cation–anion coupling versus the experimental activation energy barriers ( $E_a$ , from refs. [20,44–47]) of five lithium ionic conductors.

of the mode number toward low-frequency is greater than that toward the high-frequency modes, leading to an asymmetric redistribution of VDOS more toward low-frequency. Figure 1a,f clearly shows  $\text{Li}_7\text{P}_3\text{S}_{11}$  superionic conductor with the smallest  $E_a$  corresponds to the largest such asymmetric redistribution of VDOS upon cation–anion coupling. It is worth emphasizing that  $N_{\text{low}} - N_{\text{high}}$  of the two halides are much smaller than those of sulfides, giving a much more symmetric coupling-induced redistribution of VDOS.

We also find that Li VDOS with cation–anion mode coupling at low frequency of <1 THz (Figure 2a) strictly follow the above trend for the five lithium ionic conductors, so that ionic conductors with more Li VDOS at <1 THz correspond to smaller  $E_a$  (Figure 2c). This is not in conflict with the Einstein model,<sup>[43]</sup> in which the amplitude of thermal displacement of a mobile ion is inversely proportional to the square of vibrational frequency, and small  $E_a$  for ion diffusion is usually associated with large displacement amplitude from its equilibrium site. In contrast, Li VDOS without cation–anion mode coupling more reflects the

influence from the static environment around Li, such as the local coordination and bonding strength (Figure 2b), giving a less clean correlation with  $E_a$  due to the lack of the interactions between cation and anion vibrational modes as in the coupling case. Specifically, the poorer correlation with  $E_a$  in the non-coupled case is mainly caused by the order switch of the low-frequency mode numbers between  $\text{Li}_7\text{P}_3\text{S}_{11}$  and  $\text{Li}_{10}\text{GeP}_2\text{S}_{12}$ , which suggests the effect of coupling is especially prominent in  $\text{Li}_7\text{P}_3\text{S}_{11}$ . Although the value of 1 THz cutoff here has no absolute meaning, we notice that if the cutoff is increased to 2 THz,  $\text{Li}_{10}\text{GeP}_2\text{S}_{12}$  and  $\text{Li}_3\text{PS}_4$  in the cation–anion coupled case will slightly switch the sequence in Figure 2c with the general trend of the five compounds still being kept, thus giving a slightly less clean trend than the 1 THz cutoff. This suggests that coupled modes below 1 THz are particularly relevant to the Li-ion diffusion of the two materials of  $\text{Li}_{10}\text{GeP}_2\text{S}_{12}$  and  $\text{Li}_3\text{PS}_4$ . Note that the 1 THz cutoff found here is also very close to the low-frequency peaks from inelastic neutron diffraction measurement at 0.85 THz for  $\text{AgCrSe}_2$ , 1.2 THz for  $\text{Na}_3\text{PS}_4$ , and

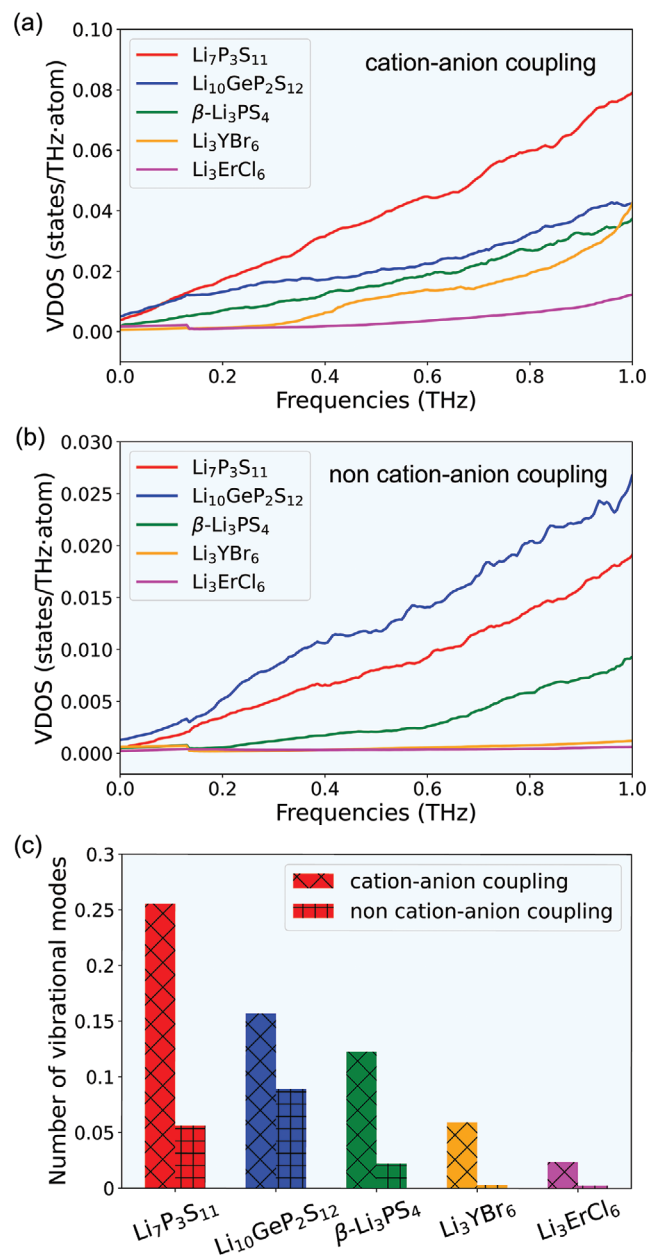


**Figure 2.** a,b) Low-frequency (<1 THz) Li VDOS of five lithium superionic conductors with and without cation–anion coupling. c) The mode number integrated from the low-frequency (<1 THz) Li VDOS with and without cation–anion coupling, respectively.

1.6 THz for  $\text{CuCrSe}_2$  superionic conductors.<sup>[16,23,24]</sup> Therefore, both the known conductivity trend of these materials and the neutron diffraction results of related materials suggest that the 1 THz cutoff is a relevant choice to the problem of interest here.

To elucidate the atomistic dynamics behind above observations, we further performed the phonon calculations for  $\text{Li}_7\text{P}_3\text{S}_{11}$ ,  $\beta\text{-Li}_3\text{PS}_4$ , and  $\text{Li}_3\text{YBr}_6$ . As illustrated in Figure 3 in the low-frequency range considerable Li vibrational modes vibrate toward the diffusion bottleneck, that is, the gate for diffusion, to maximize the hopping possibility along the right local diffusion pathway and thus are “good” for Li-ion diffusion. While

toward high-frequency ranges more Li modes vibrate toward the S–S(Br–Br) edge or along the Li–S(Br) apex, which are not diffusion pathways and thus are “bad” for Li-ion diffusion. Therefore, the relationship between VDOS redistribution and  $E_a$  discussed in Figure 1 is related to the fact that for a given material if the cation–polyanion coupling moves more vibrational modes to the low-frequency range (i.e., larger  $N_{\text{low}} - N_{\text{high}}$ ), then there will be more “good” modes for Li-ion diffusion, giving smaller  $E_a$  for the material. Note that we chose a 75% cutoff to define “good” or “bad” frequency as stated in Figure 3 caption, which simply requires that a “good” frequency should exhibit more “good” modes. If the 75% is moved to a lower value like 55%, a bit more “medium” frequency will be labeled as “good,” while the transition to “medium” frequency is still around 1 THz.

To further obtain insights into the mechanism of cation–anion mode coupling, we directly performed the anharmonic phonon coupling calculations for  $\text{Li}_7\text{P}_3\text{S}_{11}$ ,  $\beta\text{-Li}_3\text{PS}_4$ , and  $\text{Li}_3\text{YBr}_6$ , as shown in Figure 4. More details about calculating anharmonic coupling strength for a pair of phonon modes can be found in our previous works on cuprate superconductors,<sup>[40,41]</sup> where the corresponding origin from electronic band structure dynamics has also been extensively analyzed and discussed. Our calculation shows a distribution of the anharmonic cation–anion coupling strength between different mode pairs in the three lithium ionic conductors (Figure 4a,c,e). A careful analysis shows that the medium-low frequency Li vibrational modes anharmonically couple with the high-frequency polyanion vibrational modes, while the medium-high frequency Li vibrational modes prefer to anharmonically couple with the low-frequency polyanion vibrational modes, corresponding to the two peaks at negative and positive mode index differences, respectively, on the two sides of Figure 4b,d,f. The two peaks are referred as low- and high-frequency Li anharmonic peaks, respectively. The anharmonic cation–anion coupling modes with relatively high coupling strength are shown in Tables S1–S5, Supporting Information.

Furthermore, for  $\text{Li}_7\text{P}_3\text{S}_{11}$  the low-frequency Li anharmonic peak is much stronger than the high frequency one in Figure 4b, suggesting that the anharmonic Li–polyanion coupling strength for medium-low frequency Li modes are much stronger than that for the high-frequency Li modes. Thus, the VDOS redistribution upon cation–anion coupling more toward the low-frequency direction in Figure 1a is related to the stronger coupling of low-frequency Li vibrational mode with the high-frequency polyanionic vibrational modes. Particularly, these high-frequency polyanionic modes are stretching or flexing modes, as shown in Table S1, Supporting Information. Such couplings benefit lithium ionic conductivity, as they help Li oscillate with large amplitude toward the direction of diffusion channel, eventually leading to the smaller  $E_a$  of  $\text{Li}_7\text{P}_3\text{S}_{11}$ . While the high-frequency Li vibrational modes, which prefer to anharmonically couple with the low-frequency rotational modes of polyanion (Figure S1, Supporting Information), usually vibrate along or cling to the Li–S apex (Table S2, Supporting Information), indicating the rotational modes of  $\text{PS}_4$  polyanion would not help Li-ion diffusion in  $\text{Li}_7\text{P}_3\text{S}_{11}$ .

For  $\beta\text{-Li}_3\text{PS}_4$  in Figure 4d, similar trend is observed, consistent with the VDOS redistribution more toward low-frequency

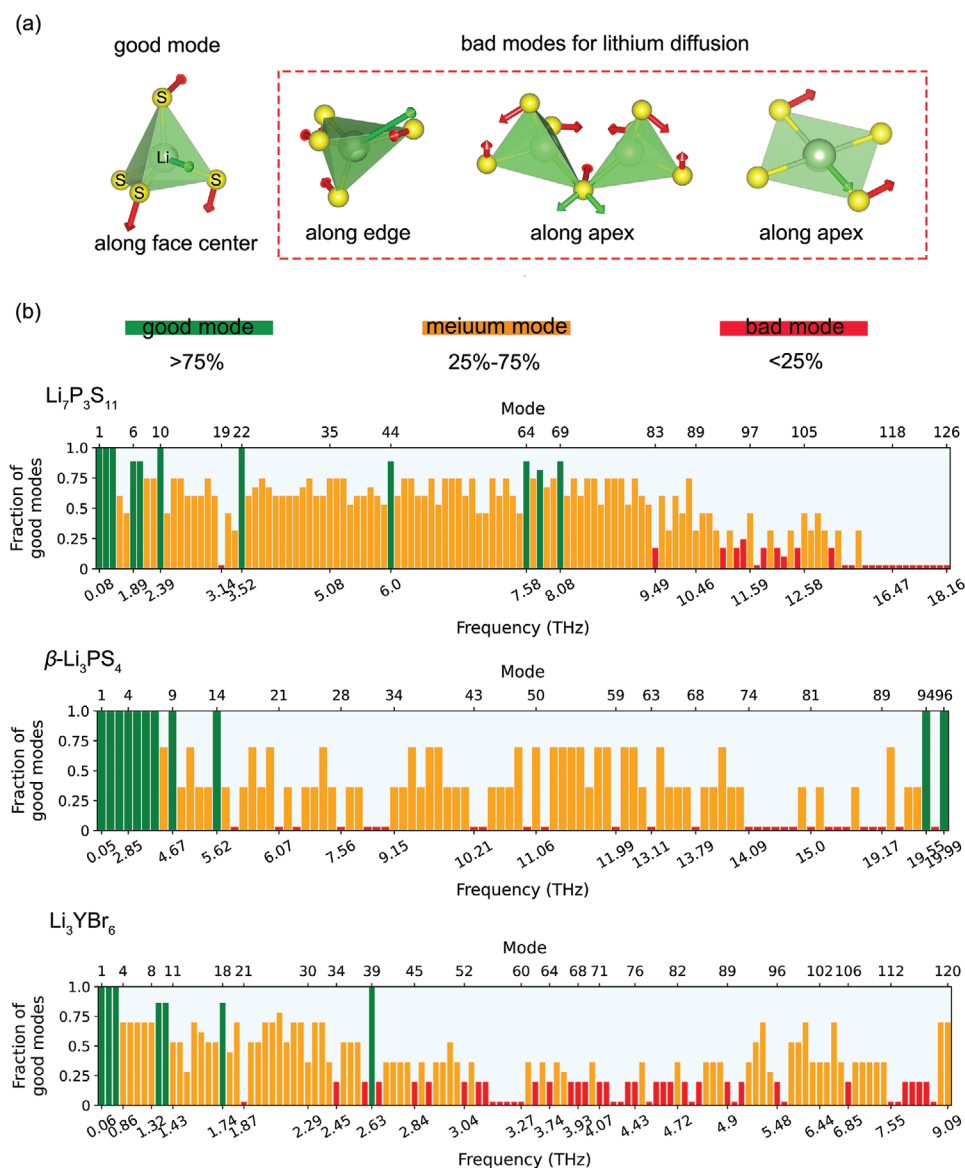


**Figure 3.** Vibrational modes for Li-ion diffusion. a) Schematic diagrams of the good and bad vibrational modes for Li-ion diffusion in  $\beta$ -Li<sub>3</sub>PS<sub>4</sub>, b) the frequency distributions of the good, medium and bad Li vibration modes, and the fraction of good Li vibrational modes at each frequency for Li<sub>7</sub>P<sub>3</sub>S<sub>11</sub>,  $\beta$ -Li<sub>3</sub>PS<sub>4</sub>, and Li<sub>3</sub>YBr<sub>6</sub>. Li vibrational modes were obtained by processing the eigenvalues of phonon calculations. The direction of the Li vibration mode along the S<sub>3</sub>(Br<sub>3</sub>) face center is good for Li-ion diffusion, while the directions of these Li vibration modes toward the S–S(Br–Br) edge and along Li–S(Br) apex are bad for Li-ion diffusion. All Li modes in lattice are considered for the vibrational direction analysis. At each frequency, if more than 75% Li modes are good for Li-ion diffusion, this vibrational frequency is colored as green. If more than 75% Li modes are bad for Li-ion diffusion, this vibrational frequency is colored as red. Other vibrational frequencies are regarded as medium modes, marked in orange color.

for Li vibrational modes (Figure 1c). However, quantitatively, the value of Li VDOS at low-frequency (<1 THz) of  $\beta$ -Li<sub>3</sub>PS<sub>4</sub>, through coupling with high-frequency polyanion stretching or flexing modes, is smaller than those of Li<sub>7</sub>P<sub>3</sub>S<sub>11</sub> and Li<sub>10</sub>GeP<sub>2</sub>S<sub>12</sub> (Figure 2), thus giving the third largest value of  $N_{\text{low}} - N_{\text{high}}$  (Figure 1f). The rotational modes of PS<sub>4</sub> polyanion are also observed in the low-frequency range, as shown in Figure S2, Supporting Information, but they nearly have no anharmonic coupling with Li-ion vibrational modes. In addition, we find that there is a special Li vibrational mode for the tetrahedral Li sites with a frequency of 11.06 THz (mode #50 of Li<sub>3</sub>PS<sub>4</sub> in

Figure 3b, vibrational structure in Table S3, Supporting Information) that shows the anharmonic coupling with almost all polyanion modes in the full-frequency range (the horizontal pink line at 11.06 THz in Figure 4c). Such phenomenon would form a trapping effect to the tetrahedral Li and worsen Li-ion diffusion.

In contrast to these two sulfides, for the halide electrolyte of Li<sub>3</sub>YBr<sub>6</sub> the low and high frequency Li anharmonic peaks are with similar strength in Figure 4f. Thereby, Li VDOS redistributions toward low-frequency and high-frequency directions are comparable, and the increased number of low- and high-frequency

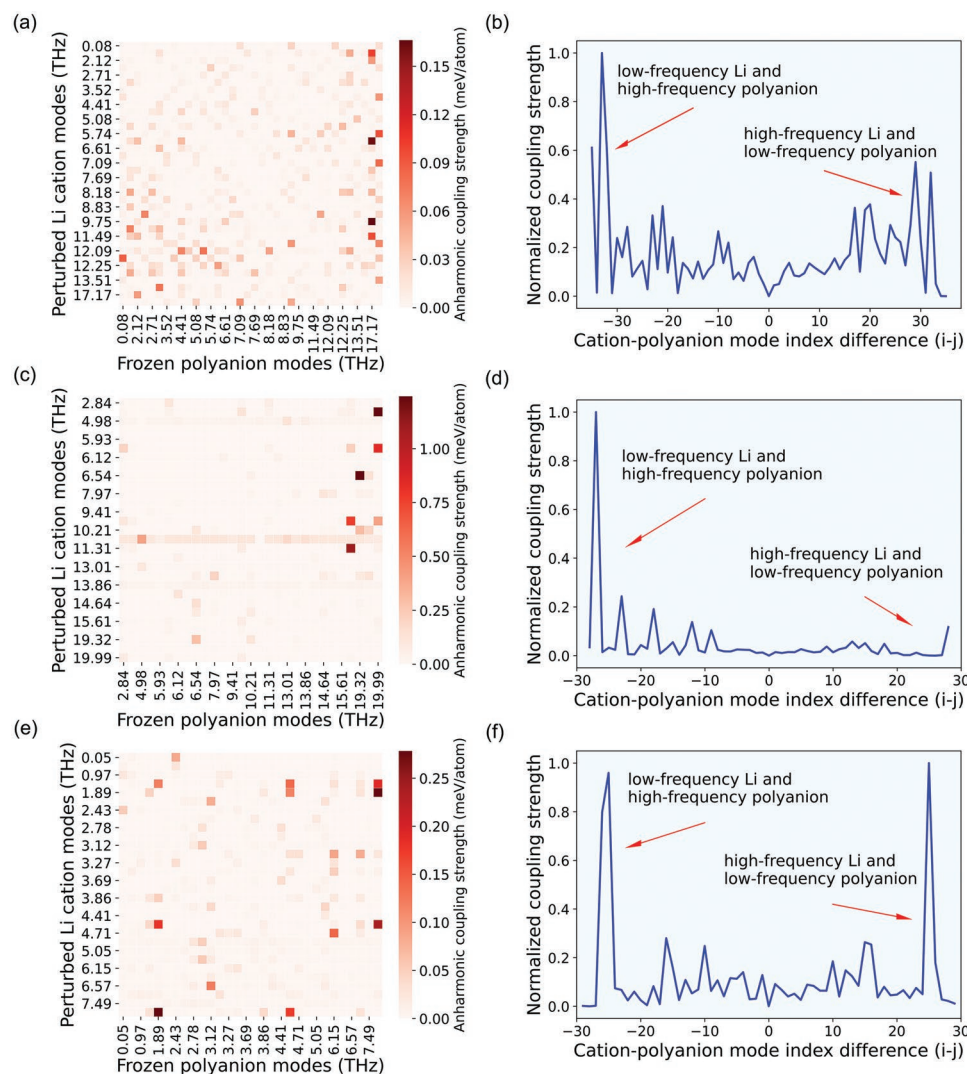


**Figure 4.** Interactions between phonon mode with anharmonic coupling. a,c,e) Anharmonic cation–polyanion phonon mode coupling for  $\text{Li}_7\text{P}_3\text{S}_{11}$  (a),  $\beta\text{-Li}_3\text{PS}_4$  (c), and  $\text{Li}_3\text{YBr}_6$  (e), respectively. b,d,f) Normalized coupling strengths of these pairs of cation–polyanion modes with the same mode index difference ( $i-j$ ,  $i$  and  $j$  are the index for cation and polyanion modes, respectively) for  $\text{Li}_7\text{P}_3\text{S}_{11}$  (b),  $\beta\text{-Li}_3\text{PS}_4$  (d), and  $\text{Li}_3\text{YBr}_6$  (f), respectively. The frequency increases with the increase of mode number. The large normalized coupling strength of the pair of cation–polyanion modes with a large negative  $i-j$  contributes to the low-frequency Li anharmonic peak, which reflects the strong coupling interaction between the low-frequency Li modes and the high-frequency polyanion modes; the large normalized coupling strength of the pair of cation–polyanion modes with a very positive  $i-j$  gives the high-frequency Li anharmonic peak, which means the strong coupling interaction between the high-frequency Li modes and the low-frequency polyanion modes.

Li vibrational modes are almost the same, leading to a very small  $N_{\text{low}} - N_{\text{high}}$  value (Figure 1f, close to zero). Furthermore, there is almost no low-frequency ( $<1$  THz) Li vibrational mode when polyanions are fixed, which is also much less than those sulfides. Even after turning on the cation–anion coupling, VDOS of the low-frequency Li modes is still far less than that of those sulfides (Figures 1 and 2). Additionally, the low-frequency Li modes coupling with the high-frequency polyanion modes have relatively small vibrational amplitude in  $\text{Li}_3\text{YBr}_6$ , as shown in Table S4, Supporting Information, suggesting that  $\text{Li}_3\text{YBr}_6$  electrolyte will benefit less from the good mode couplings to reduce  $E_a$  for lithium-ion diffusion. Moving toward high-frequency, Li vibrational modes of  $\text{Li}_3\text{YBr}_6$  anharmonically couple with the low-frequency rotational modes of  $\text{YBr}_6$  polyanion (Figure S3, Supporting Information), which are

usually medium or even bad types for Li-ion diffusion, as shown in Table S5, Supporting Information and Figure 3b, indicating that the increased high-frequency Li anharmonic peak here in comparison with sulfides (Figure 4b,d,f) would further cause an increase of  $E_a$ . These factors together may cause the generally higher  $E_a$  in halide superionic conductors than that in the sulfide ones.

### 3. Conclusions

By combining the ab initio molecular dynamics simulations with the anharmonic phonon coupling calculations, this work investigated the effects of the Li–polyanion coupling dynamics on Li-ion conduction in  $\text{Li}_7\text{P}_3\text{S}_{11}$ ,  $\text{Li}_{10}\text{GeP}_2\text{S}_{12}$ ,  $\beta\text{-Li}_3\text{PS}_4$ ,  $\text{Li}_3\text{YBr}_6$ , and  $\text{Li}_3\text{ErCl}_6$ . Viewed from Li VDOS, upon cation–anion

coupling, the number of medium-frequency Li vibration modes decreases and the number of both low- and high-frequency modes increases. It is found that the smaller  $E_a$  of Li-ion diffusion in the sulfide-based lithium superionic conductors are often related to the asymmetric redistribution of more Li VDOS toward the low-frequency vibrational direction, driven by the anharmonic coupling with the high-frequency polyanion stretching or flexing modes, through which Li ions are pushed by the coupled modes moving toward the main diffusion channels for reduced diffusion barrier. In contrast, in halides, the increased number of low- and high-frequency Li vibrational modes are comparable upon cation–anion coupling, because of comparable low- and high-frequency Li anharmonic peaks. Additionally, the coupling between low-frequency Li and high-frequency polyanion modes in  $\text{Li}_3\text{YBr}_6$  shows relatively small vibrational amplitudes, suggesting that halide electrolytes will benefit less from such good mode couplings to reduce  $E_a$  for Li-ion diffusion. The trend predicted here among these materials agrees well with the known experimental trend of their ionic conductivities, further suggesting the importance of the proposed mechanism.

Importantly, we find that the rotational modes of polyanion at low-frequency anharmonically couple with the high-frequency Li vibrational modes, which would not help Li-ion diffusion. It is also worth noting that although the beneficial effect for hopping due to the large amplitude of low-frequency Li phonon mode may in principle be diminished by the reduced jumping attempt frequency in the pre-exponential term for conductivity, the additional anharmonic coupling of the low frequency Li mode with high frequency stretching or flexing polyanion modes found in this work can help the Li diffusion. Specifically, the anharmonic coupling may help increase the successful rate of the attempt, as it makes the Li move directly toward the diffusion channel, and also help maintain the attempt frequency at a relatively high level in a soft lattice, due to the coupling with the high frequency modes. These are additional factors that can also contribute to higher conductivity, in addition to the reduced  $E_a$ . Such coupling might contribute to similar low-frequency peak as observed from inelastic neutron diffraction measurements of Na, Ag, Cu-ion-based superionic conductors at low temperatures.<sup>[16,23,24]</sup> We suggest more systematic experiments and computations to investigate such Li–polyanion anharmonic coupling dynamics for Li-ion diffusion, as it may lead to a new “anharmonic descriptor” for the design of advanced superionic conductors upon a deeper understanding.

## 4. Experimental Section

All calculations were carried out in the framework of density functional theory (DFT)<sup>[48]</sup> using the projector augmented wave method,<sup>[49]</sup> as implemented in the Vienna Ab initio Simulation Package (VASP). The generalized gradient approximation (GGA)<sup>[50]</sup> and Perdew–Burke–Ernzerhof (PBE) exchange functional<sup>[48]</sup> was employed. Structural relaxations were performed by using the spin-polarized GGA method,<sup>[51]</sup> and the plane-wave energy cutoff was set to 520 eV. The Monkhorst–Pack method<sup>[52]</sup> with the  $k$ -points meshes of  $4 \times 2 \times 2$ ,  $3 \times 3 \times 2$ ,  $4 \times 3 \times 2$ ,  $2 \times 2 \times 2$ , and  $2 \times 2 \times 2$  were employed for the Brillouin zone sampling, respectively for the structural relaxation calculations of unit-cells of  $\text{Li}_7\text{P}_3\text{S}_{11}$ ,  $\text{Li}_{10}\text{GeP}_2\text{S}_{12}$ ,  $\beta\text{-Li}_3\text{PS}_4$ ,  $\text{Li}_3\text{ErCl}_6$ , and  $\text{Li}_3\text{YBr}_6$ . The convergence criteria of energy and force were set to  $10^{-5}$  eV atom<sup>-1</sup> and 0.05 eV Å<sup>-1</sup>, respectively.

The VDOS of lithium ions (polyanions) were calculated by the Fourier transform of the corresponding velocity–velocity autocorrelation function from the AIMD simulations, which fully included the anharmonicity and temperature effects.<sup>[53,54]</sup> Li VDOS were normalized by the number of the total Li vibrational modes in the simulated cell, that is, integrating the normalized Li VDOS within the whole frequency range would get a value equal to three times the number of Li ion ( $3N_{\text{Li}}$ ). The number of Li VDOS at the low-frequency range ( $N_{\text{low}}$ ) was calculated by integrating the normalized Li VDOS from zero to an upper limit that was determined by the intersection of the two Li VDOS curves at the low-frequency range with and without cation–anion coupling. Similarly, the number of Li VDOS at the high-frequency range ( $N_{\text{high}}$ ) was calculated by integrating the normalized Li VDOS from a lower limit at the other intersection of the two curves at high frequency to infinity. All AIMD calculations were performed without spin-polarization in an NVT canonical ensemble at elevated temperatures with a Nose–Hoover thermostat.<sup>[55]</sup> A smaller plane wave energy cut-off of 300 eV was chosen for AIMD simulations of the supercells with a Gamma-centered  $1 \times 1 \times 1$   $k$ -point grid, and the simulation supercell sizes were at least 10 Å along each lattice direction. Time step was set to 2 fs, and all supercell systems were simulated for a short time with a total of 50 000 steps.

Generally, there was little difference of phonon DOS distribution between room temperature and 0 K, such as Al,<sup>[56]</sup> FeSi,<sup>[57]</sup> and GaN<sup>[58]</sup> systems, and previously checked solid electrolyte systems in either simulation or experiment,<sup>[11,12]</sup> which justified the relevance of the phonon calculation at 0 K to the room temperature AIMD result and experimental report. The phonon calculations were performed based on the density functional perturbation theory, as implemented in the Phonopy code.<sup>[59]</sup> The phonon modes were enumerated at the Gamma point in the unit cells of  $\text{Li}_7\text{P}_3\text{S}_{11}$ ,  $\beta\text{-Li}_3\text{PS}_4$ , and  $\text{Li}_3\text{YBr}_6$ . For  $\text{Li}_7\text{P}_3\text{S}_{11}$ , 36 representative phonon modes out of the total 126 modes were selected for the anharmonic phonon coupling calculations. The other modes were excluded for phonon coupling calculation because they have similar atom movements to the selected representative modes and the limited computational sources. Similarly, 30 out of 96 modes and 30 out of 120 modes, respectively for  $\beta\text{-Li}_3\text{PS}_4$  and  $\text{Li}_3\text{YBr}_6$  were selected for the anharmonic phonon coupling calculations. For each pair of cation–polyanion phonons, Li ions were chosen as the “perturbation mode” and polyanion as the “frozen mode”. The atomic vibrational amplitudes from the normal phonon calculations were added to both the frozen mode and perturbation mode in lattice. Seven dependent self-consistent field (SCF) calculations were performed on each perturbation mode with the scaled amplitude of  $-0.6$ ,  $-0.4$ ,  $-0.2$ ,  $0$ ,  $0.2$ ,  $0.4$ , and  $0.6$ , respectively. The seven SCF energies were used to fit a parabola energy profile. If the two modes had no anharmonic coupling, the energy potential would follow the term of  $\frac{1}{2}\omega^2Q^2$  ( $\omega$  and  $Q$  denote the frequency and normal coordinate of mode, respectively) describing harmonic oscillations, and the energy minimum of this potential profile would be at  $Q = 0$  amplitude of the perturbation mode, as depicted in Figure S4, Supporting Information. If there was an anharmonic coupling, the minimum of the fitted parabola profiles would shift to a non-zero amplitude, and the absolute energy of the equilibrium position was defined as the strength of anharmonic phonon coupling, as depicted in Figure S4, Supporting Information. More method details of calculating anharmonic coupling strength for a pair of phonon modes could be found in the previous work on cuprate superconductors.<sup>[40,41]</sup>

## Supporting Information

Supporting Information is available from the Wiley Online Library or from the author.

## Acknowledgements

This work is partially supported by Data Science Initiative Competitive Research Award at Harvard University, Climate Change Solutions Fund

at Harvard University, and partially supported by the Assistant Secretary for Energy Efficiency and Renewable Energy (EERE), Vehicle Technology Office (VTO) of the U.S. Department of Energy (DOE) through the Advanced Battery Materials Research (BMR) program. Z.X. thanks China Scholarship Council (CSC) for support as a visiting scholar for one year at Harvard. H.Z. thanks the National Natural Science Foundation of China (52072240). This work was supported by computational resources from the Extreme Science and Engineering Discovery Environment (XSEDE) Stampede and Frontera supercomputers.

## Conflict of Interest

The authors declare no conflict of interest.

## Data Availability Statement

The data that support the findings of this study are available from the corresponding author upon reasonable request.

## Keywords

anharmonic coupling, diffusion dynamics, ionic conductors, stretching mode, vibrational density of states

Received: August 14, 2022

Revised: October 16, 2022

Published online:

- [1] A. Manthiram, X. Yu, S. Wang, *Nat. Rev. Mater.* **2017**, 2, 16103.
- [2] C. Sun, J. Liu, Y. Gong, D. P. Wilkinson, J. Zhang, *Nano Energy* **2017**, 33, 363.
- [3] Q. Zhang, D. Cao, Y. Ma, A. Natan, P. Aurora, H. Zhu, *Adv. Mater.* **2019**, 31, 1901131.
- [4] Y. Wang, L. Ye, X. Chen, X. Li, *JACS Au* **2022**, 2, 886.
- [5] L. Ye, X. Li, *Nature* **2021**, 593, 218.
- [6] Y. Wang, W. D. Richards, S. P. Ong, L. J. Miara, J. C. Kim, Y. Mo, G. Ceder, *Nat. Mater.* **2015**, 14, 1026.
- [7] X. He, Q. Bai, Y. Liu, A. M. Nolan, C. Ling, Y. Mo, *Adv. Energy Mater.* **2019**, 9, 1902078.
- [8] D. Di Stefano, A. Miglio, K. Robeyns, Y. Filinchuk, M. Lechartier, A. Senyshyn, H. Ishida, S. Spannenberger, D. Prutsch, S. Lunghammer, D. Rettenwander, M. Wilkening, B. Roling, Y. Kato, G. Hautier, *Chem* **2019**, 5, 2450.
- [9] X. He, Y. Zhu, Y. Mo, *Nat. Commun.* **2017**, 8, 15893.
- [10] Z.-H. Fu, X. Chen, N. Yao, X. Shen, X.-X. Ma, S. Feng, S. Wang, R. Zhang, L. Zhang, Q. Zhang, *J. Energy Chem.* **2022**, 70, 59.
- [11] S. Muy, J. C. Bachman, L. Giordano, H.-H. Chang, D. L. Abernathy, D. Bansal, O. Delaire, S. Hori, R. Kanno, F. Maglia, S. Lupart, P. Lamp, Y. Shao-Horn, *Energy Environ. Sci.* **2018**, 11, 850.
- [12] A. K. Sagotra, D. Chu, C. Cazorla, *Phys. Rev. Mater.* **2019**, 3, 035405.
- [13] J. G. Smith, D. J. Siegel, *Nat. Commun.* **2020**, 11, 1483.
- [14] Z. Zhang, H. Li, K. Kaup, L. Zhou, P.-N. Roy, L. F. Nazar, *Matter* **2020**, 2, 1667.
- [15] Z. Zhang, P. N. Roy, H. Li, M. Avdeev, L. F. Nazar, *J. Am. Chem. Soc.* **2019**, 141, 19360.
- [16] M. K. Gupta, J. Ding, N. C. Osti, D. L. Abernathy, W. Arnold, H. Wang, Z. Hood, O. Delaire, *Energy Environ. Sci.* **2021**, 14, 6554.
- [17] T. Krauskopf, S. Muy, S. P. Culver, S. Ohno, O. Delaire, Y. Shao-Horn, W. G. Zeier, *J. Am. Chem. Soc.* **2018**, 140, 14464.
- [18] J. C. Bachman, S. Muy, A. Grimaud, H. H. Chang, N. Pour, S. F. Lux, O. Paschos, F. Maglia, S. Lupart, P. Lamp, L. Giordano, Y. Shao-Horn, *Chem. Rev.* **2016**, 116, 140.
- [19] S. Muy, R. Schlem, Y. Shao-Horn, W. G. Zeier, *Adv. Energy Mater.* **2020**, 11, 2002787.
- [20] S. Muy, J. Voss, R. Schlem, R. Koerver, S. J. Sedlmaier, F. Maglia, P. Lamp, W. G. Zeier, Y. Shao-Horn, *iScience* **2019**, 16, 270.
- [21] M. A. Kraft, S. P. Culver, M. Calderon, F. Bocher, T. Krauskopf, A. Senyshyn, C. Dietrich, A. Zevalkink, J. Janek, W. G. Zeier, *J. Am. Chem. Soc.* **2017**, 139, 10909.
- [22] T. Famprikis, J. A. Dawson, F. Fauth, O. Clemens, E. Suard, B. Fleutot, M. Courty, J.-N. Chotard, M. S. Islam, C. Masquelier, *ACS Mater. Lett.* **2019**, 1, 641.
- [23] J. Ding, J. L. Niedziela, D. Bansal, J. Wang, X. He, A. F. May, G. Ehlers, D. L. Abernathy, A. Said, A. Alatas, Y. Ren, G. Arya, O. Delaire, *Proc. Natl. Acad. Sci. U. S. A.* **2020**, 117, 3930.
- [24] J. L. Niedziela, D. Bansal, A. F. May, J. Ding, T. Lanigan-Atkins, G. Ehlers, D. L. Abernathy, A. Said, O. Delaire, *Nat. Phys.* **2018**, 15, 73.
- [25] A. B. Kvist, A. Bengtzelius, in *Fast Ion Transport in Solids: Solid State Batteries and Devices*, (Ed.: W. van Gool), North-Holland Publishing Company, Amsterdam, The Netherlands **1973**, pp. 193–199.
- [26] M. Jansen, *Angew. Chem. Int. Ed.* **1991**, 30, 1547.
- [27] L. Nilsson, J. O. Thomas, B. C. Tofield, *J. Phys. C: Solid State Phys.* **1980**, 13, 6441.
- [28] R. Kaber, L. Nilsson, N. H. Andersen, A. Lunden, J. O. Thomas, *J. Phys.: Condens. Matter* **1992**, 4, 1925.
- [29] A. Lundén, *Solid State Ionics* **1988**, 28–30, 163.
- [30] D. Blanchard, A. Nale, D. Sveinbjörnsson, T. M. Eggenhuisen, M. H. W. Verkuijlen, Suwarno, T. Vegge, A. P. M. Kentgens, P. E. de Jongh, *Adv. Funct. Mater.* **2015**, 25, 184.
- [31] K. E. Kweon, J. B. Varley, P. Shea, N. Adelstein, P. Mehta, T. W. Heo, T. J. Udovic, V. Stavila, B. C. Wood, *Chem. Mater.* **2017**, 29, 9142.
- [32] N. Verdál, T. J. Udovic, V. Stavila, W. S. Tang, J. J. Rush, A. V. Skripov, *J. Phys. Chem. C* **2014**, 118, 17483.
- [33] C. S. Babu, B. L. Tembe, *Chem. Phys. Lett.* **1992**, 194, 351.
- [34] N. Andersen, P. Bandaranayake, M. Careem, M. Dissanayake, C. Wijayasekera, R. Kaber, A. Lunden, B. Mellander, L. Nilsson, J. Thomas, *Solid State Ionics* **1992**, 57, 203.
- [35] E. A. Secco, *J. Solid State Chem.* **1992**, 96, 366.
- [36] R. W. Impey, M. L. Klein, I. R. McDonald, *J. Chem. Phys.* **1985**, 82, 4690.
- [37] J. Huang, L. Zhang, H. Wang, J. Zhao, J. Cheng, Weinan E, *J. Chem. Phys.* **2021**, 154, 094703.
- [38] S. Muy, J. C. Bachman, H.-H. Chang, L. Giordano, F. Maglia, S. Lupart, P. Lamp, W. G. Zeier, Y. Shao-Horn, *Chem. Mater.* **2018**, 30, 5573.
- [39] K. Wakamura, *Phys. Rev. B* **1997**, 56, 11593.
- [40] S. Kim, X. Chen, W. Fitzhugh, X. Li, *Phys. Rev. Lett.* **2018**, 121, 157001.
- [41] X. Chen, J. Dong, X. Li, *NPJ Comput. Mater.* **2020**, 6, 103.
- [42] R. Mankowsky, A. Subedi, M. Forst, S. O. Mariager, M. Chollet, H. T. Lemke, J. S. Robinson, J. M. Glowina, M. P. Minitti, A. Frano, M. Fechner, N. A. Spaldin, T. Loew, B. Keimer, A. Georges, A. Cavalleri, *Nature* **2014**, 516, 71.
- [43] M. T. Dove, *Introduction to Lattice Dynamics*, Cambridge University Press, New York **1993**.
- [44] Y. Seino, T. Ota, K. Takada, A. Hayashi, M. Tatsumisago, *Energy Environ. Sci.* **2014**, 7, 627.
- [45] N. Kamaya, K. Homma, Y. Yamakawa, M. Hirayama, R. Kanno, M. Yonemura, T. Kamiyama, Y. Kato, S. Hama, K. Kawamoto, A. Mitsui, *Nat. Mater.* **2011**, 10, 682.
- [46] T. Asano, A. Sakai, S. Ouchi, M. Sakaida, A. Miyazaki, S. Hasegawa, *Adv. Mater.* **2018**, 30, 1803075.



- [47] Z. Liu, W. Fu, E. A. Payzant, X. Yu, Z. Wu, N. J. Dudney, J. Kiggans, K. Hong, A. J. Rondinone, C. Liang, *J. Am. Chem. Soc.* **2013**, *135*, 975.
- [48] W. Kohn, L. J. Sham, *Phys. Rev.* **1965**, *140*, A1133.
- [49] P. E. Blöchl, *Phys. Rev. B* **1994**, *50*, 17953.
- [50] J. P. Perdew, K. Burke, M. Ernzerhof, *Phys. Rev. Lett.* **1996**, *77*, 3865.
- [51] S. L. Dudarev, G. A. Botton, S. Y. Savrasov, C. J. Humphreys, A. P. Sutton, *Phys Rev B* **1998**, *57*, 1505.
- [52] H. J. Monkhorst, J. D. Pack, *Phys. Rev. B* **1976**, *13*, 5188.
- [53] E. v. d. M. Niek, J. J. de Klerk, . Wagemaker, *ACS Appl. Energy Mater.* **2018**, *1*, 3230.
- [54] Z. Xu, Y. Xia, *J. Mater. Chem.* **2022**, *10*, 11854.
- [55] W. G. Hoover, *Phys. Rev. A* **1985**, *31*, 1695.
- [56] M. Kresch, M. Lucas, O. Delaire, J. Y. Y. Lin, B. Fultz, *Phys. Rev. B* **2008**, *77*, 024301.
- [57] O. Delaire, I. I. Al-Qasir, J. Ma, A. M. dos Santos, B. C. Sales, L. Mauger, M. B. Stone, D. L. Abernathy, Y. Xiao, M. Somayazulu, *Phys. Rev. B* **2013**, *87*, 184304.
- [58] J. E. Herriman, O. Hellman, B. Fultz, *Phys. Rev. B* **2018**, *98*, 214105.
- [59] A. Togo, I. Tanaka, *Scr. Mater.* **2015**, *108*, 1.